



**HAL**  
open science

## Optimization of SLIPI–polarization ratio imaging for droplets sizing in dense sprays

S. Garcia, Mehdi Stiti, P. Doublet, C. Lempereur, M. Orain, E. Berrocal

► **To cite this version:**

S. Garcia, Mehdi Stiti, P. Doublet, C. Lempereur, M. Orain, et al.. Optimization of SLIPI–polarization ratio imaging for droplets sizing in dense sprays. *Experiments in Fluids*, 2024, 65 (6), pp.96. 10.1007/s00348-024-03830-z . hal-04621976

**HAL Id: hal-04621976**

**<https://ut3-toulouseinp.hal.science/hal-04621976>**

Submitted on 24 Jun 2024

**HAL** is a multi-disciplinary open access archive for the deposit and dissemination of scientific research documents, whether they are published or not. The documents may come from teaching and research institutions in France or abroad, or from public or private research centers.

L'archive ouverte pluridisciplinaire **HAL**, est destinée au dépôt et à la diffusion de documents scientifiques de niveau recherche, publiés ou non, émanant des établissements d'enseignement et de recherche français ou étrangers, des laboratoires publics ou privés.



Distributed under a Creative Commons Attribution 4.0 International License



# Optimization of SLIPI–polarization ratio imaging for droplets sizing in dense sprays

S. Garcia<sup>1</sup> · M. Stiti<sup>2,3</sup> · P. Doublet<sup>1</sup> · C. Lempereur<sup>1</sup> · M. Orain<sup>1</sup> · E. Berrocal<sup>3</sup>

Received: 25 August 2023 / Revised: 7 May 2024 / Accepted: 18 May 2024 / Published online: 7 June 2024  
© The Author(s) 2024

## Abstract

In this article, structured laser illumination planar imaging and polarization ratio techniques are successfully combined to size droplets in various optically dense sprays. The polarization ratio approach is based on the acquisition of the perpendicular and parallel polarized components of Lorenz–Mie scattered light, for which the ratio is proportional to the surface mean diameter,  $D_{21}$ . One of the main advantages of this technique, compared to some other laser imaging techniques for particle sizing, is that no fluorescent dye is required. This makes the technique suitable for characterizing sprays under evaporation conditions, such as combustion or spray drying applications. In addition, the SLIPI technique aims at suppressing the detection of multiple light scattering and at extracting the desirable single-light scattering signal. To test the reliability of this novel approach, an industrial hollow-cone nozzle is used, injecting at 50 bar water mixed with Glycerol (in the range of 0–60%). The first aim of this work is to study the experimental parameters that influence the reliability of the technique, such as the polarization orientation of the incident light, the refractive index of the injected liquid and the variation of the droplet size distribution. Using Phase Doppler Anemometry, the results show that a linear calibration is obtained for droplets ranging between 10 and 70  $\mu\text{m}$ , when the incident illumination has a polarization set to 10° and 20°. In addition, this article demonstrates the feasibility of the technique for the measurement of liquids having a refractive index reaching 1.41. In the last stage of this work, after rotating the nozzle every 5°, a 3D tomographic reconstruction of  $D_{21}$  is performed. This demonstrates the robustness and efficiency of the technique for droplet sizing in 3D, under challenging conditions.

## 1 Introduction

According to Rayleigh, a spray is characterized as a collection of droplets in a gas-filled environment (Rayleigh 1878). Sprays serve a wide range of applications, including liquid fuel injection in combustion engines, industrial powder production via spray drying, as well as for some specific medical treatments. The ability to measure spray characteristics holds fundamental importance, helping to improve and control the optimization of systems using spray-based technologies. Regarding combustion science, the knowledge of spray quantities such as droplet size distribution and mean

diameter is of utmost importance for the understanding of the subsequent liquid–air mixing and evaporation processes (Ashgriz 2011) (Lefebvre and McDonell 2017).

To measure these quantities experimentally, two laser-based diagnostics are mainly available in the literature: point measurements (Durst and Zaré 1975) (Bachalo 1980) and 2D imaging (Berrocal et al. 2023). Phase doppler anemometry (PDA) is the most commonly used method for determining the droplet size and velocity (Bachalo and Houser 1987; Lacoste et al. 2003; Hage et al. 2010). Despite providing good accuracy, this calibration-free method is limited to point measurements, which makes the technique time-consuming for the characterization of a whole spray. In order to overcome this limitation, laser sheet imaging techniques offer an alternative solution, allowing for high spatial resolution and fast measurements. For droplet sizing, laser sheet imaging is mainly based on intensity ratio measurements, such as the polarization ratio technique (Hofeldt 1993a; Hofeldt 1993b), the LIF/Mie technique (LIF for Laser Induced Fluorescence and Mie for the Lorenz–Mie scattering signal) (Yeh et al. 1993;

✉ E. Berrocal  
edouard.berrocal@fysik.lu.se

<sup>1</sup> Département Multi-Physique pour l’Énergétique (DMPE), ONERA, Université de Toulouse, Toulouse, France

<sup>2</sup> Institut de Mécanique des Fluides de Toulouse (IMFT), CNRS, Université de Toulouse, Toulouse, France

<sup>3</sup> Division of Combustion Physics, Department of Physics, Lund University, Lund, Sweden

Domann and Hardalupas 2003) and the Raman/Mie technique (Malarski et al. 2009). When using these methods, the signal ratio is proportional to a statistical mean droplet diameter (Mugele and Evans 1951). Theoretically, the LIF/Mie and the Raman/Mie techniques yield a ratio proportional to the Sauter mean diameter (SMD or  $D_{32}$ ).

The LIF/Mie technique is often related to the use of an excitation wavelength in the visible range (Le Gal et al. 1999; Domann and Hardalupas 2003), leading to the need of adding a dye in the injected liquid. This limits the measurement to non-evaporating sprays. To suppress the fluorescence signal from the vapor phase of evaporating sprays, the exciplex method LIEF/Mie can be used (Zeng et al. 2012; Qiu et al. 2023). However, under certain hot evaporating conditions the amount of dye may not contribute to the gas phase but instead increase in concentration in droplets, leading to a significant signal variation during the measurement time (Frackowiak and Tropea 2010). This increase of dye in significant proportions can also alter the physical properties of the fluid, such as surface tension and viscosity (Stiti et al. 2021). The polarization ratio is a good alternative technique for 2D droplet sizing in evaporating sprays because it does not require a fluorescence signal. This is based on the calculation of the ratio between the perpendicular (*s*-pol;  $\beta = 90^\circ$ ) and parallel (*p*-pol;  $\beta = 0^\circ$ ) polarized scattered lights providing a statistical surface mean diameter ( $D_{21}$ ).

In practice, intensity-based techniques depend on parameters such as laser excitation wavelength, refractive index, scattering angle and particle size. As demonstrated in the literature, these parameters affect the respective proportions of the light intensity ratio and mean diameter (Massoli et al. 1989; Charalampous and Hardalupas 2011a, b; Bareiss et al. 2013). A calibration procedure is applied by comparing the intensity ratio with the results obtained by a PDA instrument in a steady-state spray (Sankar et al. 1999; Le Gal et al. 1999), or by using a monodisperse droplet generator that accurately controls the droplet diameter within the range of interest (Koegl et al. 2018a, b).

In sprays of low optical density, where single light scattering predominates, laser imaging can directly provide quantitative results (Garcia et al. 2023). However, in optically dense sprays, additional scattering events occur leading to unwanted contributions (Berrocal et al. 2005a; b) (Lehnert et al. 2023):

1. The signal generated from the laser sheet can be multiply scattered on its way to the camera (along a path normal to the laser sheet).
2. The laser sheet widens along the incident path through the spray due to multiple light scattering in semi-forward direction. This broadening of the illumination generates a signal out of the intended plane.

A technique based on the use of spatially modulated laser sheet, called SLIPI (Structured Laser Illumination Planar Imaging) (Berrocal et al. 2008; Kristensson et al. 2008), suppresses efficiently all the unwanted light described in the contribution 1 and most of it described in the contribution 2. The technique has been applied to various liquid injection systems including hollow cones (Kristensson et al. 2010), air assisted (Wellander et al. 2011), diesel (Berrocal et al. 2012) and direct-injection spark-ignition (DISI) (Koegl et al. 2019) sprays. In addition, SLIPI can also be used for the three-dimensional (3D) reconstruction, by collecting 2D planes shifted in space (Wellander et al. 2011; Mishra et al. 2019). In a recent study (Stiti et al. 2023), it has been demonstrated for the first time that the polarization ratio technique is successfully applicable to optical dense sprays when coupled with the SLIPI method.

The aim of the work presented in this article is to perform an experimental and numerical analysis of the parameters influencing the polarization ratio technique and to provide insights and limitations of the technique for future particle sizing of dense atomizing sprays. The remainder of the paper consists of five sections:

- The first section revisits the theoretical background of the technique and conducts numerical Lorenz–Mie simulations to demonstrate its applicability to a polydisperse spray.
- In the second section, a detailed description of the experimental setup is presented, featuring the utilization of a telecentric lens and a fully integrated beam splitter device. Additionally, the post-processing routine for generating polarization ratio map is outlined in this section.
- The third section undertakes an experimental analysis of the impact of incident laser polarization orientation on the reliability of the polarization ratio with the  $D_{21}$  droplet size.
- In the fourth section, the study focuses on the polarization ratio measurement capabilities for different complex refractive indices ( $n = n_r + ik$ ). Both numerical (MiePlot simulations) and experimental studies are employed.
- Finally, an optimal configuration of SLIPI–polarization ratio is defined and the measurement of  $D_{21}$  is achieved in 3D on an industrial transient water spray running at 50 bar injection pressure. Those measurements are achieved by rotating the injector and doing a tomographic reconstruction.

## 2 Theoretical background of polarization ratio droplet sizing

The first applications of the polarization ratio technique were presented in early 1980th, where the results were related to the use of isothermal sprays and to combustion applications

(Beretta et al. 1981, 1983, 1985). In Beretta and co-workers work, the physical understanding of light scattering by droplets is limited to the interpretation of the angular scattering coefficient  $\mu_s(\theta)$  [ $\text{m}^{-1}$ ] which is directly proportional to  $N$  [ $\#/\text{m}^3$ ], corresponding to the number of droplets by volume unit (Beretta et al. 1985):

$$\mu_s(\theta) = N\sigma_s(\theta, n, D) \tag{1}$$

where  $\sigma_s(\theta, n, D)$  is the angular scattering cross-section [ $\text{m}^2$ ], which is a function of the scattering angle  $\theta$  [ $^\circ$ ], the droplet diameter  $D$  [ $\text{m}$ ] and the complex refractive index  $n$  (Van de Hulst 1981).

Two physical interpretations can be attributed to the scattering cross-section: first, it corresponds to the ratio between the total flux of light scattered by a droplet  $W_s$  [ $\text{W}$ ] and the incident light flux density  $I_i$  [ $\text{W}/\text{m}^2$ ]; second, it can be interpreted as a geometrical cross-section receiving the incident energy and scattering it according to an efficiency factor  $Q$ :

$$\sigma_s(\theta, n, D) = \frac{W_s(\theta, n, D)}{I_i} = Q(\theta, n)\sigma_g(D) \tag{2}$$

where  $\sigma_g$  [ $\text{m}^2$ ] is the geometrical cross-section which depends on the observed droplet diameter  $D$  [ $\text{m}$ ] ( $\sigma_g = \pi D^2/4$ ).

Using this approach, Massoli and co-workers, or even Hofeldt and Hanson, extended the technique to the application of the polarization ratio technique to single droplet sizing (Massoli et al. 1989; Hofeldt and Hanson 1991). The polarization ratio is obtained by analyzing the signal produced by individual droplets, at an observation angle of  $\theta = 90^\circ$ . The authors demonstrated that, over a large size range (10–200  $\mu\text{m}$ ), the  $s$ -pol signal is proportional to the projected surface area ( $D^2$ ), whereas the  $p$ -pol signal is proportional to the diameter ( $D$ ). By applying an  $s$ -pol/ $p$ -pol ratio, it is thus possible to recover a value close to  $D_{21}$ . However, the strong oscillations in the light scattered by micrometric spherical droplets prevent any direct correlation between size and scattered intensity (Hofeldt 1993a; b). These Lorenz–Mie oscillations are caused by the interference of light scattered from different refractive orders interacting within a single droplet. A solution to this problem was found by Beretta and co-workers, who studied the effects of absorption on polarization ratio technique using numerical methods (Beretta et al. 1985). They demonstrated, for a single droplet, that the surface waves are progressively damped as the absorption index increases. Indeed, in the case of a transparent sphere, the wave mostly travels in a lossless medium. However, if the droplets are no longer transparent, part of the energy is absorbed and the surface waves are more strongly damped and consequently the oscillations in the scattered intensity decrease. The major drawback with this solution is that, for liquids with a low absorption rate at the excitation wavelength (e.g., water at 532 nm), a dye must

be added. An alternative solution is the use of ultra-short laser pulses to significantly reduce the oscillations from the scattering phase functions (Bakic et al. 2008). To solve this issue femtosecond laser pulses can be used for droplet sizing based on the polarization ratio technique (Bareiss et al. 2013). The results of this study confirm that the time and coherence length of the incident laser light influence the development of Lorenz–Mie signal ripples. All of this preliminary research on the polarization ratio technique relates to single droplets. However, according to Hofeldt (1993a), with a polydisperse spray where the intensity-based scattered measurements are derived from a statistical droplet size passing through the measurement volume, the strong oscillations induced by the large droplets are also attenuated by the contribution of the smaller droplets. These results can be demonstrated numerically by calculating the scattered light from a sphere using the Lorenz–Mie theory and the Debye series. Laven developed a computer program (Laven 2008), called “MiePlot”, using a simple interface, based on the classic BHMIE algorithm (Bohren and Huffman 1983).

In the case of a polydisperse spray, where the droplet sizes can be described by a distribution function  $f(D)$ , Eq. (1) can be rewritten for each polarized scattering coefficients:

$$\mu_{\perp}(\theta) = \int_0^{\infty} N\sigma_{\perp}(\theta, n, D)f(D)dD \propto N \int_0^{\infty} D^2f(D)dD \tag{3}$$

$$\mu_{\parallel}(\theta) = \int_0^{\infty} N\sigma_{\parallel}(\theta, n, D)f(D)dD \propto N \int_0^{\infty} Df(D)dD \tag{4}$$

where  $\sigma_{\perp}(\theta, n, D)$  and  $\sigma_{\parallel}(\theta, n, D)$  are the  $s$ -pol and  $p$ -pol scattering cross-section, respectively.

Simulations were carried out using the MiePlot software to demonstrate the dependence indicated in Eqs. 3 and 4, as shown in Fig. 1a, b. The input data for this code are the real ( $n_r$ ) and imaginary ( $ik$ ) parts of the refractive index, the laser excitation wavelength  $\lambda$ , the scattering angle  $\theta$ , the laser polarization ( $s$ -pol,  $p$ -pol or Unpolarized) and the diameter range of the droplet  $D$  (single droplets or polydisperse distributions). The results show the simulated Lorenz–Mie scattered intensity for  $s$ -pol and  $p$ -pol polarization as a function of droplet diameter in 1–100  $\mu\text{m}$  range. A scattering angle of  $90^\circ$ , a center wavelength of  $\lambda = 532$ , a refractive index of  $n = 1.33 + 0i$  (pure water) and a diameter resolution of  $\Delta\theta = 0.05 \mu\text{m}$  are used for the calculations, corresponding to the experiments described in the second section of this paper. For monodisperse diameter distributions, the results show strong ripples for large droplets. However, these strong oscillations can be reduced by the polydispersion of a spray, as shown in Fig. 1 (b). In the polydisperse simulation, the mean diameter is given

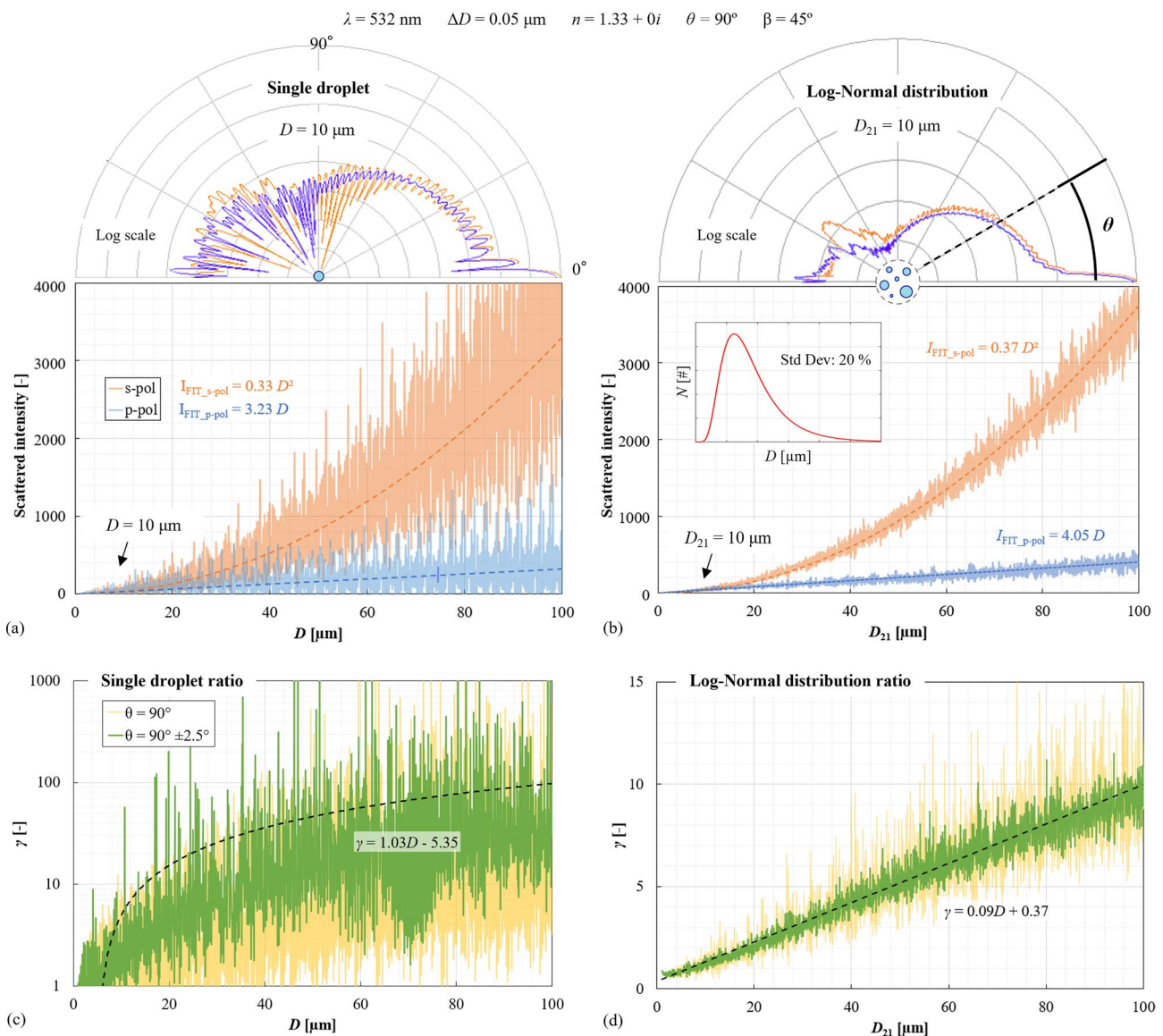


**Fig. 1** MiePlot simulations of the Lorenz–Mie scattered signals *s*-pol and *p*-pol, as a function of water droplet diameter when considering single droplets in (a) and polydisperse size distributions in (b). The related polarization ratio  $\gamma$  is respectively given in (c) and (d),

without aperture (in yellow) and with an aperture angle of  $\Delta\theta=5^\circ$  (in green). The ratio is obtained with an incident light polarization oriented at  $\beta 45^\circ$  (50% *s*-pol and 50% *p*-pol). For better readability, the vertical scale on c is plotted on a logarithmic scale

along the x-axis, assuming a log-normal distribution with a standard deviation of 20% and using 20 points in the distribution. This type of droplet size distribution is typically observed in simple x-type pressurized injectors, similar to the one employed in this article. Hence, this distribution hypothesis is utilized here as an initial approximation. The signal detection is assumed as a point receiver located at  $90^\circ$  scattering angle where an additional aperture ( $\pm 2.5^\circ$ ) is also considered to simulate the collection angle  $\Delta\theta=5^\circ$  of the telecentric lens used in the experiment. It can be observed in Fig. 1c, d that the collection angle reduces the oscillations. However, the theoretical residual uncertainty

remains evident and is imposed by the presence of ripples which increases for larger droplets. In addition, a reduction of ripples in the scattering phase function can be observed when the polydispersity is considered in the simulation. On the one hand, for single droplet applications, the results show a nonlinear relation between polarization ratio  $\gamma$  and diameter  $D$  (the best fit is given by the linear trend given on the graphic:  $\gamma = 1.03D - 5.35$ ). On the other hand, for polydisperse configurations, the results show a quasi-linear relation between ratio and mean diameter (the best fit is given by the linear trend given on the graphic:  $\gamma = 0.09D + 0.37$ ).

To further investigate the theoretical relationship between the polarization ratio and  $D_{21}$ , the influence of the droplet size distribution function is studied. Three log-normal distributions with different standard deviations ( $\sigma_1 = 0.01\%$ ,  $\sigma_2 = 1\%$ , and  $\sigma_3 = 20\%$ ) and two bimodal distributions (a narrow one and a broad one) are used to compute the ratio. The results are illustrated in Fig. 2. Notably, significant oscillations are observed for the log-normal distribution with  $\sigma_1 = 0.01\%$ . In this case, the results are similar to those obtained using single droplets. This type of monodisperse distribution is not representative of the spray investigated experimentally. Conversely, for models with  $\sigma = 1\%$  and  $20\%$ , the oscillations are substantially reduced, and the curves nearly superimpose on each other. Moreover, the results from the two bimodal distributions align closely with those of the log-normal models. To quantify the differences between each distribution, a comparison is realized, where the ratio values are derived for different diameters.

As shown in the “Bimodal vs Log-normal distribution” in Fig. 2, the discrepancy of the ratio values increases with diameter. Specifically, there is an observed variation in the range of ratio values of about 7% for small diameter (i.e.,  $D_{21} = 10 \mu\text{m}$ ), while it reaches 58% for large diameter (i.e.,  $D_{21} = 80 \mu\text{m}$ ). Additionally, the results indicate ratio values higher for a log-normal distribution. This observation suggests that the significant presence of large droplets may affect the accuracy of the ratio, particularly for higher  $D_{21}$  values ( $> 50 \mu\text{m}$ ). For example, in the case of a log-normal distribution for a  $D_{21} = 60 \mu\text{m}$  and a standard deviation  $\sigma_3 = 20\%$ , it is possible to find several droplets above  $100 \mu\text{m}$ , unlike the other distributions where diameters do not exceed  $90 \mu\text{m}$ . Hence, the shape of the particle size distribution seems to significantly influences the value of the ratio.

As previously stated, the polarization ratio technique is based on the calculation of the ratio of the vertical ( $s$ -pol) and horizontal ( $p$ -pol) polarized Lorenz–Mie scattered signals. Using now an imaging system, where a detection volume is imaged which contains a certain number of droplets with different diameters, the signals of the individual droplets ( $k$ ) recorded by each pixel ( $i, j$ ) are ensemble averaged. Considering the signal emitted by the droplets as a scattered flux density, the ratio of the two perpendicular and parallel polarized scattered intensities can be written as follows:

$$\gamma_{ij} = \left( \frac{I_{\perp s}}{I_{\parallel s}} \right)_{ij} = \frac{C_{\perp} \sum_k N_{ij} D_{ij}^2}{C_{\parallel} \sum_k N_{ij} D_{ij}} = C(D_{21})_{ij} \quad (5)$$

where  $I_{\perp s}$  and  $I_{\parallel s}$  are the  $s$ -pol and  $p$ -pol scattered intensity,  $N_{ij}$  is the number of particles of size  $k$  captured in the pixel of coordinates ( $i, j$ ),  $C_{\perp}$  and  $C_{\parallel}$  are two constants experimentally determined by a calibration. The intensity ratio measured in each map pixel is therefore proportional to the local

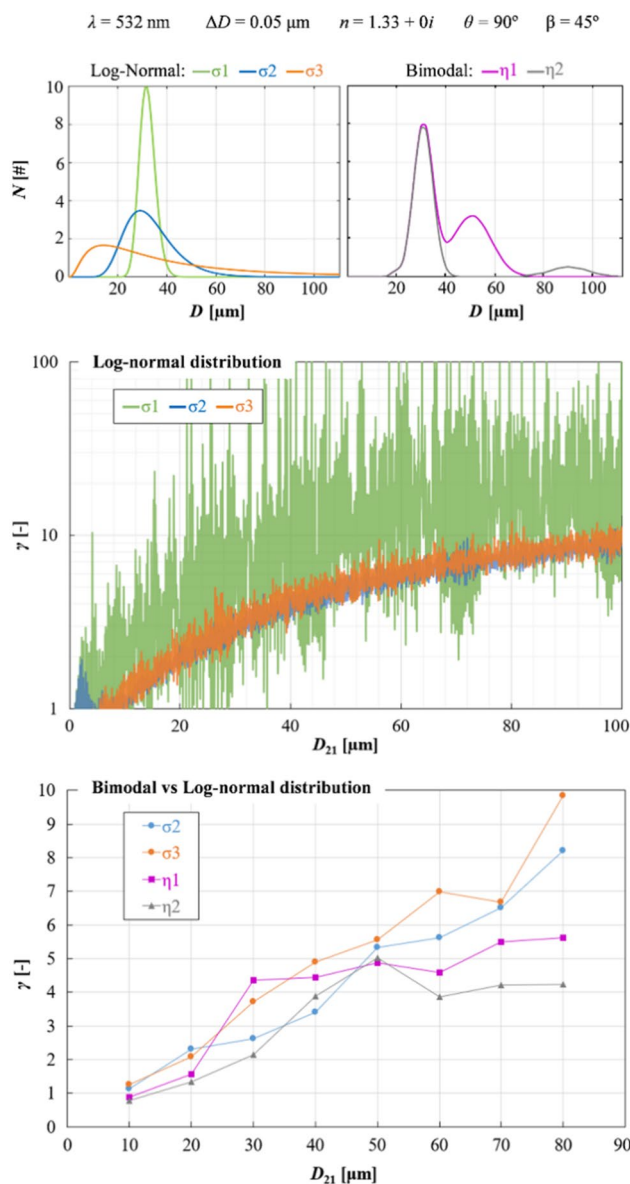


**Fig. 2** Polarization ratio  $\gamma$  as a function of  $D_{21}$  for various particle size distributions: log-normal ( $\sigma_1 = 0.01\%$ ,  $\sigma_2 = 1\%$ , and  $\sigma_3 = 20\%$ ) and bimodal. Each simulation is computed with  $\theta = 90^\circ$  and an aperture angle of  $\Delta\theta = 5^\circ$ . The evolution of the polarization ratio is shown (plots on the bottom) by assuming four particle size distributions

surface mean diameter,  $D_{21}$  (Lefebvre and McDonell 2017). Note that experimentally, there is variation of light intensity that is related to:

- Non-uniformity of the laser beam profile (different light intensity at different locations)
- Variation of light intensity over time (different light intensity between each recordings)
- Effects of light extinction along the incident direction (there is much more light at the entrance of the spray than at the exit)

- Effects of light extinction between the laser sheet and the camera (various loss of light on the way to the camera as the droplet concentration is highly inhomogeneous)

However, as the two polarized images are simultaneously recorded with the same field-of-view, they are both affected in the same way. Thus, their ratio allows to efficiently suppressed unwanted effects related to any light intensity variation.

### 3 Description of the experiment

#### 3.1 SLIPI–polarization ratio optical setup

The optical setup of the SLIPI–polarization ratio is described in Fig. 3. A continuous laser (Spectra-Physics Millennia Prime, 532 nm, 5 W) is used to illuminate the droplets. The beam is converted into a structured laser sheet of 12-cm high and 2-mm thick, by a combination of spherical and cylindrical lenses. A diffractive optical element (DOE) is also used to produce a spatially modulated intensity along the vertical direction of the planar illumination. The top of laser sheet is located 2 cm downstream from the injector exit,

which ensures that areas where the spray is not fully formed (related to the spray formation region) are not considered.

A steady-state water hollow-cone spray, generated by a pressure swirl atomizer (Tetra Pak injector, simplex model, Flow Number =  $23 \text{ L h}^{-1} \text{ bar}^{-1/2}$ ), is investigated in atmospheric conditions. Liquid injection pressure is set to 50 bar, which leads to a volume flow-rate of 2.7 L/min for water. Under these injection conditions, the droplet density  $N$  [ $\#/\text{m}^3$ ] is such that multiple light scattering is predominant in the spray, preventing intensity-based measurements without the use of a SLIPI module. Measurements with the same injection system were previously presented by Stiti and co-workers, yielding optical depth (OD) values larger than 1 (Stiti et al. 2023).

The light intensity is modulated using a diffractive optical element (DOE) (Holo/Or, DS-190 532), acting as a light-efficient Ronchi grating. The 3p-SLIPI method is implemented to maintain the spatial resolution offered by the detection setup (Berrocal et al. 2008). Three images, modulated and phase-shifted by  $2\pi/3$ , must be acquired for the purpose of reconstructing the final image using the 3p-SLIPI method. Each phase is displaced by vertically transferring the DOE using a piezoelectric motor (PiMotor). A zero-order air-spaced  $\lambda/2$  polarizer (Thorlabs, Half-Wave Plates,

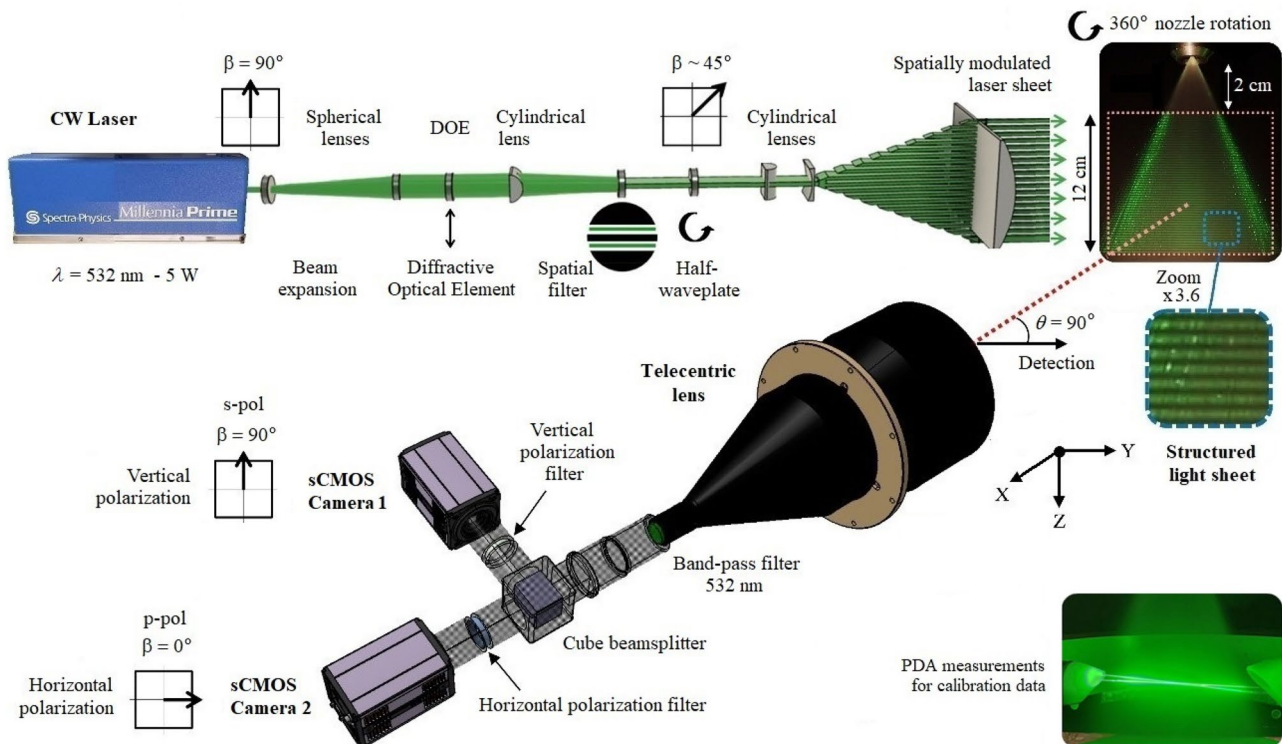


**Fig. 3** Scheme of the experimental setup for 3p-SLIPI–polarization ratio measurement. A spatially modulated light sheet is generated by means of a diffractive optical element. The incident light is polarized at a  $45^\circ$  angle using a half-waveplate. Scattered signals are collected

by a telecentric lens (positioned at  $\theta = 90^\circ$ ), and images corresponding to parallel and perpendicular polarizations are captured on two cameras using a beamsplitter cube and two polarizing filters

WPHSM05-532) is coupled with the 3p-SLIPI device and used to adjust the polarization axis of the incident beam. The polarizer is placed at an angular orientation of  $\beta=45^\circ$  as a first approximation referring to the previous work of (Bareiss et al. 2013; Stiti et al. 2023). The reception module is placed at a scattering angle of  $90^\circ$ . The scattering signal is recorded using a large telecentric objective (0.066X, 1" C-Mount TitanTL<sup>®</sup>), with an aperture angle of  $\Delta\theta=5^\circ$ . As shown by (Garcia et al. 2023), a telecentric lens is used to remove the angular dependence of the scattered Mie signal in the field-of-view: all the light rays collected have a scattering angle  $\theta=90^\circ$ . The particularities of a telecentric lens are a fixed magnification at any object distance and a large depth of field. Two sCMOS cameras (Andor, Zyla 5.5) are used and coupled to the lens by a TwinCam module (CAIRN research). The two cameras are synchronized using an Arduino module (Uno Rev3) which receives the acquired data and transmits to the two cameras simultaneously. A 532 nm specific band-pass filter (Thorlabs, FLH0532-1) is fitted on the telecentric lens to filter the TwinCam input signal. A beam splitter cube (Thorlabs, non-polarizing 50/50, BS013) is used to distribute the signal equally between the two cameras. Polarization filters (Thorlabs, LPVISC100b, OD6) are placed in front of each camera and oriented as necessary to collect the required polarization for each sensor.

Various methods can be used to calibrate intensity ratios from planar laser imaging techniques. An ex situ method consists of using a monodisperse droplet generator that accurately controls the droplet diameter in the range of interest (Bareiss et al. 2013; Mishra et al. 2019). Signals from the droplets are recorded sequentially as a function of droplet diameter, and the correlation between intensity ratio and droplet diameter is used for calibration purposes. The major disadvantage of this method is that a monodisperse injection system must be added to the experiments, and the optical setup must be adapted to a much smaller field-of-view. An in situ method consists of creating a calibration function (also called look-up table in our previous article (Garcia et al. 2023)) to relate mean diameter values measured with a PDA system and the intensity ratios deduced from image processing at the same points (Le Gal et al. 1999). The technique is effective, but it requires a second optical diagnostic technique. In this paper, the in situ calibration method is chosen. Thus, PDA measurements are taken using an Artium PDI TK2 to calibrate the polarization ratio and validate the conversion to  $D_{21}$ .

### 3.2 Post-processing routine

The acquisition and post-processing routine for the  $s$ -pol and  $p$ -pol images is carried out using a custom-made interface developed on the App Designer from MATLAB. All the maps presented in this paper are based on the acquisition

and averaging of three modulated images ( $I_0$ ,  $I_{120}$  and  $I_{240}$ ), where the phase of the sinusoidal modulation of the intensity is shifted by  $120^\circ$  corresponding to a third of the modulation period. For each phase, sixty images using a long exposure time of 80 ms are recorded. The final image of light intensity  $I_{\text{SLIPI}}$  is obtained using the following equation (Berrocal et al. 2008):

$$I_{\text{SLIPI}} = \frac{\sqrt{2}}{3} \cdot \sqrt{(I_0 - I_{120})^2 + (I_0 - I_{240})^2 + (I_{120} - I_{240})^2} \quad (6)$$

Figure 4 shows comparisons between conventional  $s$ -pol and  $p$ -pol ( $I_{\text{Conv}}$ ) and SLIPI ( $I_{\text{SLIPI}}$ ) images. The laser sheet propagates from left to right, and, as can be seen, in both cases the laser signal is attenuated across the spray due to large droplet density. The polarization ratio  $\gamma$  is then reconstructed according to Eq. 5, for  $I_{\text{Conv}}$  and  $I_{\text{SLIPI}}$ . On  $I_{\text{Conv}}$ , the hollow-cone spray shape characteristic of the injector used in the paper is not observed, whereas this shape is visible on  $I_{\text{SLIPI}}$ , which demonstrates the benefits of the SLIPI technique in terms of removing the multiple scattering effects.

In order to remove the influence of the cameras noise, a "dark" image is defined and applied on each average  $s$ -pol and  $p$ -pol image. To define a physical scale on each average image, a calibration is then realized (1 px correspond to 0.07 mm). The TwinCam system allows a physical superimposition of the optical paths (error:  $\pm 1$  px). The application of the ratio on the whole  $s$ -pol and  $p$ -pol images produces an aberrant result outside of the spray area, so a mask is defined and applied on the map. A calibration is then applied to the ratio image in order to define the  $D_{21}$  maps. As the injector is mounted on a rotating system ( $360^\circ$ ), 2D measurements of the polarization ratio at different angles (from  $0^\circ$  to  $90^\circ$  with a  $5^\circ$  step) are recorded, which allows the reconstruction of a 3D spray image. The different planes are then assembled in a 3D matrix, according to a common reference system corresponding to the injection axis. Linear interpolations are then performed between the measurement planes to complete the 3D matrix. The matrix is then exported to the ParaView software which allows the visualization of the results. In this way, spray cross-sections can be deduced from the interpolation of the longitudinal data. For a better understanding, all these operations are summarized in Table 1.

## 4 Experimental analysis of various polarization angles from the incident light

Recent work (Koegl et al. 2022) has shown that the polarization of the incident light influences the proportionality between the Lorenz–Mie signal and droplet diameter. Further investigation is undertaken here to study the influence of the incident light polarization on the SLIPI–polarization



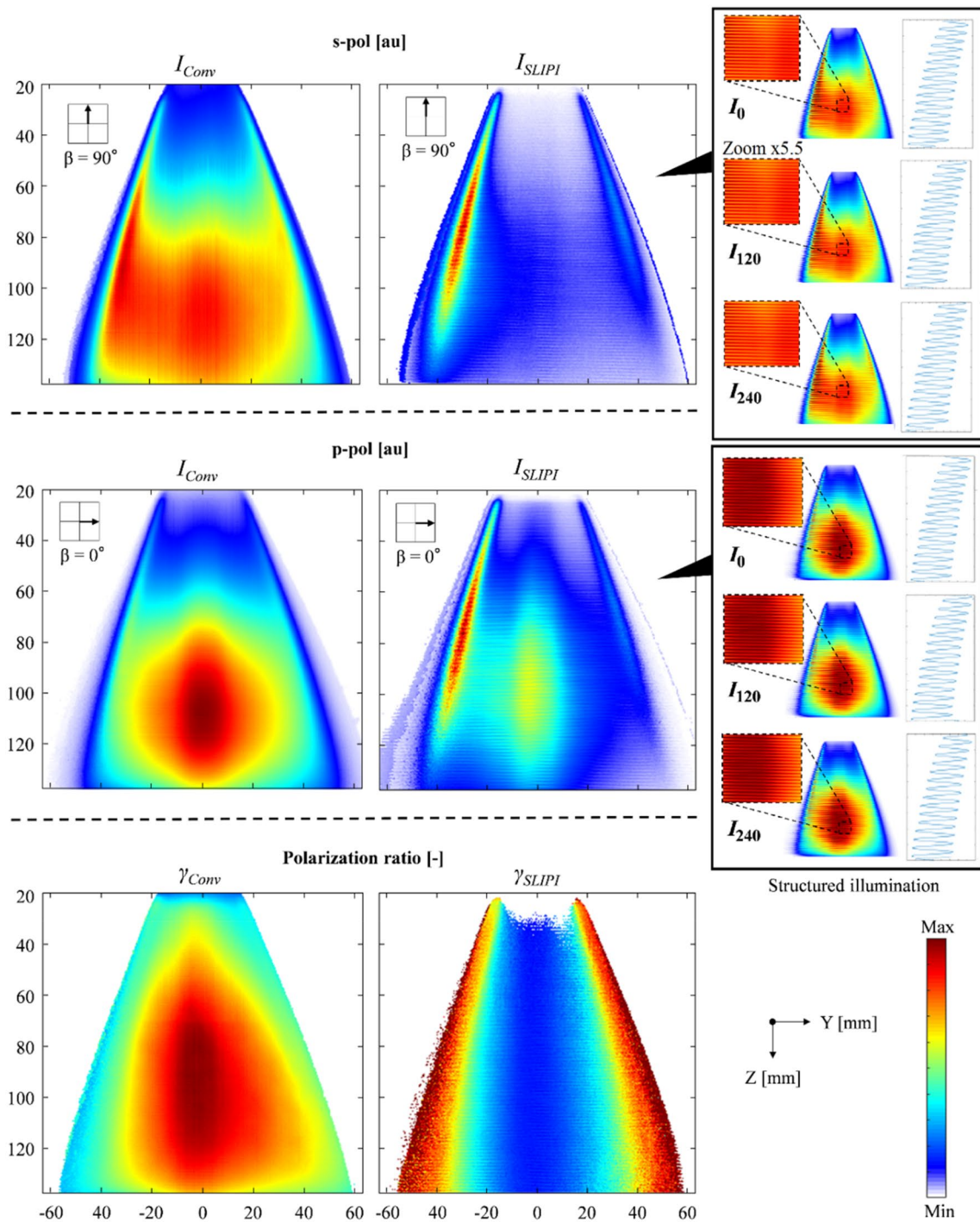


**Fig. 4** Averaged *s*-pol and *p*-pol images of a hollow-cone spray injecting at 50 bar water spray are produced by capturing three spatial modulated sub-images (shown on the right). These images are taken with a 120° phase shift and SLIPI images (ISLIPI) are obtained using

Eq. 6. To demonstrate SLIPI’s ability to eliminate the effects of multiple scattering, conventional images (*I*<sub>Conv</sub>) are obtained using a traditional light sheet technique. Finally, the ratio  $\gamma$  is reconstructed according to Eq. 5

technique. Figure 5 and Fig. 6 present in the left side, different polarization ratio average maps recorded for an injection pressure of 50 bar and different incident light polarization (measurement accurate to  $\beta = \pm 1^\circ$ ). To calibrate these

polarization ratio average maps, PDA measurements are carried out at three distances from the injector ( $Z = 50$  mm, 70 mm and 90 mm), in order to build the calibration function over the largest possible range of diameters. For each

**Table 1** Different steps of the post-processing routine

N°	Steps
<i>2D map</i>	
1	Acquisition of 60 instantaneous <i>s</i> -pol and <i>p</i> -pol images for each SLIPI phases. Average for each phase and 3p-SLIPI processing (see Eq. (6) and Fig. 4)
2	Creation of a mask from a threshold on the <i>s</i> -pol and <i>p</i> -pol 3p-SLIPI images, allowing to limit the calculation to the region of the spray
3	Calculation of the <i>s</i> -pol/ <i>p</i> -pol image. Conversion of the ratio image into $D_{21}$ map
<i>3D map</i>	
4	Measurement of the $D_{21}$ for each plane ( $0^\circ$ – $90^\circ$ with a $5^\circ$ step)
5	3D matrix reconstruction using a linear interpolation between measurement planes

distance, PDA measurements are performed over a half-spray traverse on the incoming side of the laser sheet. Data are acquired every millimeter and are validated when 100,000 droplets are acquired for each measurement point. A maximum diameter gradient can thus be captured on the *Y*-axis (from 10 to 80  $\mu\text{m}$ ). Intensity profiles are then considered at the same *Z* distances on the polarization ratio image and a cloud of experimental points can be plotted.

In most studies (Bareiss et al. 2013; Stiti et al. 2023) the incident light polarization that is experimentally employed is oriented at  $\beta \approx 45^\circ$  in order to equalize the vertical and horizontal components of the illumination. As seen in Fig. 5d, for diameters below  $D_{21} = 30 \mu\text{m}$ ,  $\gamma$  values exhibit limited discrepancy, whereas above this diameter, a large discrepancy is observed that increases with diameter (for example, at  $D_{21} = 60 \mu\text{m}$  the polarization ratio method gives a  $\gamma$  range from 1.5 to 3). To investigate this phenomenon, different angles are imposed on the incident light polarization, in order to obtain an optimal configuration where the polarization ratio linearly varies with  $D_{21}$ . For  $\beta = 90^\circ$  (*s*-pol), the vertical component of polarization is detected; while for  $\beta = 0^\circ$  (*p*-pol), the horizontal component of polarization is detected.

In Fig. 5, for  $\beta > 45^\circ$  (mostly *s*-pol signal), the relationship is not bijective, which prevents any calibration. However, the absolute value of the measured ratio is larger than for  $\beta = 45^\circ$ : at  $\beta = 55^\circ$  (Fig. 5c), the maximum value is 6.5, increasing to 14.5 at  $\beta = 70^\circ$  (Fig. 5b). This tendency can be explained by the fact that for  $\beta > 45^\circ$ , the majority of the received polarization is perpendicular. As numerically demonstrated by (Stiti et al. 2023), when the incident light polarization is unbalanced between *s*-pol and *p*-pol, the dominant polarization influences the mean value of the ratio and its fluctuations. Here, the dominant polarization is the *s*-pol, and as observed in Fig. 1, for a given diameter, the mean intensity and its fluctuations are larger than those for the *p*-pol. Furthermore, as shown in Fig. 2, there is an effect of the distribution shape on the ratio value, which increases with  $D_{21}$ . As shown in Fig. 7, three shapes of droplet size distributions were measured by PDA. Each

distribution has the same  $D_{21} = 60 \mu\text{m}$ , although measured at three different *Z* distances from the injector. The results illustrate a log-normal shape at distance  $Z = 50 \text{ mm}$  and two bimodal shapes for  $Z = 70$  and  $90 \text{ mm}$ . The significant variations in the ratio observed with a  $D_{21} > 60 \mu\text{m}$  for the calibration function in Fig. 5d may also be potentially related to the change in the distribution shape. It is therefore advisable to conduct PDA measurements on each new spray to quantify the error associated with the shape of the distribution. Finally, when the incident signal is almost perpendicular (Fig. 5a), the trend reverses, and the result becomes aberrant: the smallest ratios correspond to the largest diameters.

Taking things further, angles of  $\beta < 45^\circ$ , where the polarization is mostly parallel, are then tested (Fig. 6). As a result, the relationship between ratio and diameter tends to become bijective and discrepancy of the ratio is significantly reduced for large diameters. In addition, there is a considerable decrease of the ratio for  $\beta < 45^\circ$ , due to the higher proportion of *p*-pol. For example, for  $D_{21} = 20 \mu\text{m}$  a ratio of 1.5, 0.55 and 0.1 is observed, respectively, for a  $\beta$  value of  $35^\circ$ ,  $20^\circ$  and  $10^\circ$  (Fig. 6a–c). However, a large experimental uncertainty remains for large diameters: for example, in the case of  $\beta = 35^\circ$ , the error on  $D_{21}$  is  $\pm 2 \mu\text{m}$  for  $\gamma$  equal to 0.5 and increases to  $\pm 20 \mu\text{m}$  for  $\gamma$  equal to 1.2 (Fig. 6a). As the relationship is bijective for  $\beta < 45^\circ$ , several calibration functions can be fitted, starting close to 0 because in theory, when  $D_{21} = 0 \mu\text{m}$ , the polarization ratio  $\gamma = 0$ . Consequently, the calibration function is established based on a linear equation originating close to 0, aiming to encompass a broader range of data within the curve. This linearity in the observed correlations is highly interesting compared to the nonlinear trends identified in the LIF/Mie technique (Koegl et al. 2018a, b; Garcia et al. 2023). Indeed, a linear law means that the measurement uncertainty remains constant, and the ratio between small and large diameters remains proportional. From this calibration function, a relative error (RE) of the  $D_{21}$  measurement can be calculated as follows for each diameter bin:

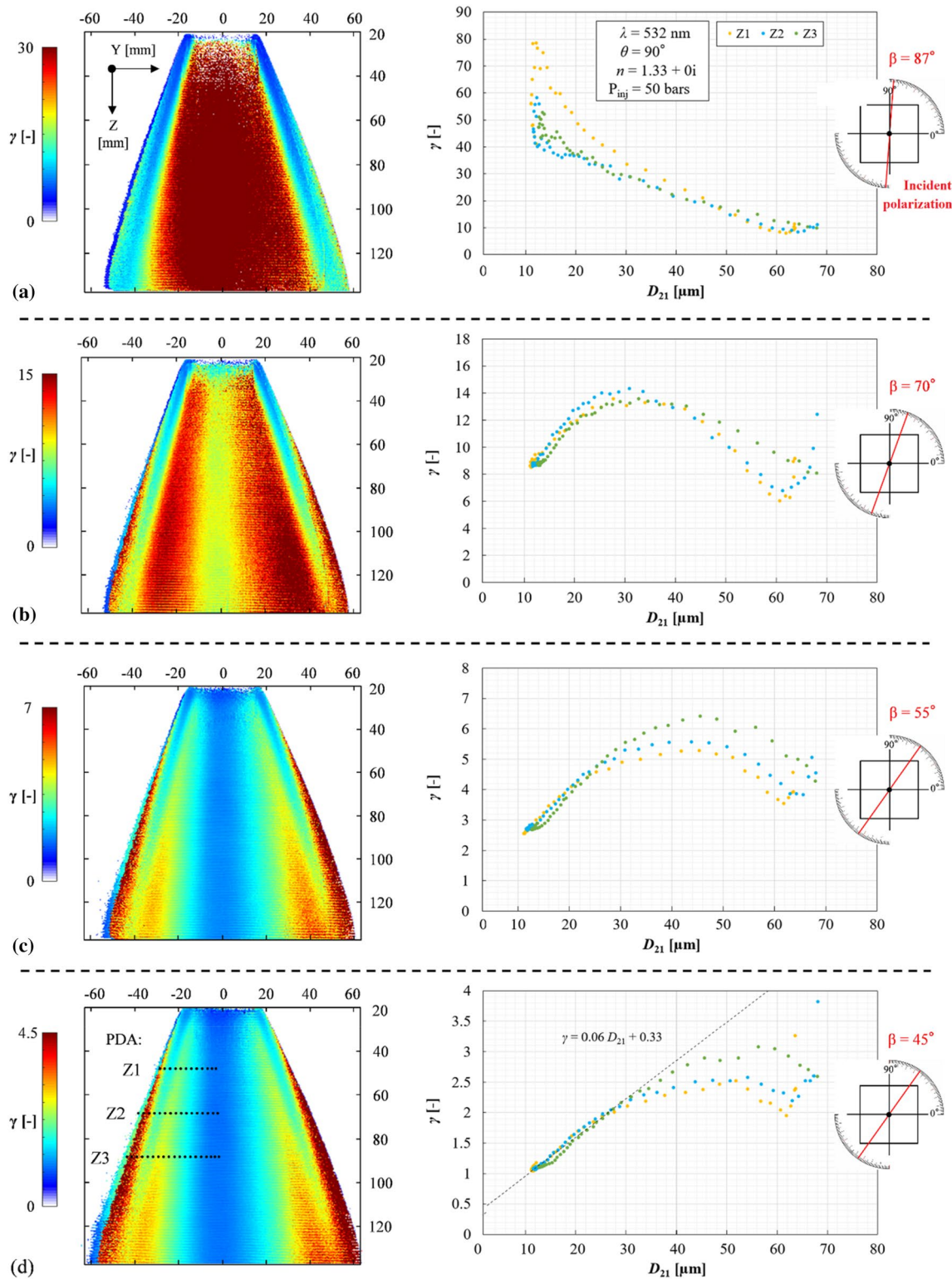


**Fig. 5** Influence of different incident light polarization ( $\beta$ =**a** 87°, **b** 70°, **c** 55° and **d** 45°), on the polarization ratio. On the left-hand side, different average ratio maps of the water hollow-cone spray, obtained for an injection pressure of  $P_{inj}=50$  bar. The laser sheet propagates from left to right. Positions of the PDA measurement volume are dis-

played at different distances from the injector:  $Z1=50$  mm,  $Z2=90$  mm and  $Z3=90$  mm. On the right-hand side, different calibration functions correlating  $\gamma$  to the surface mean diameter  $D_{21}$  measured by PDA

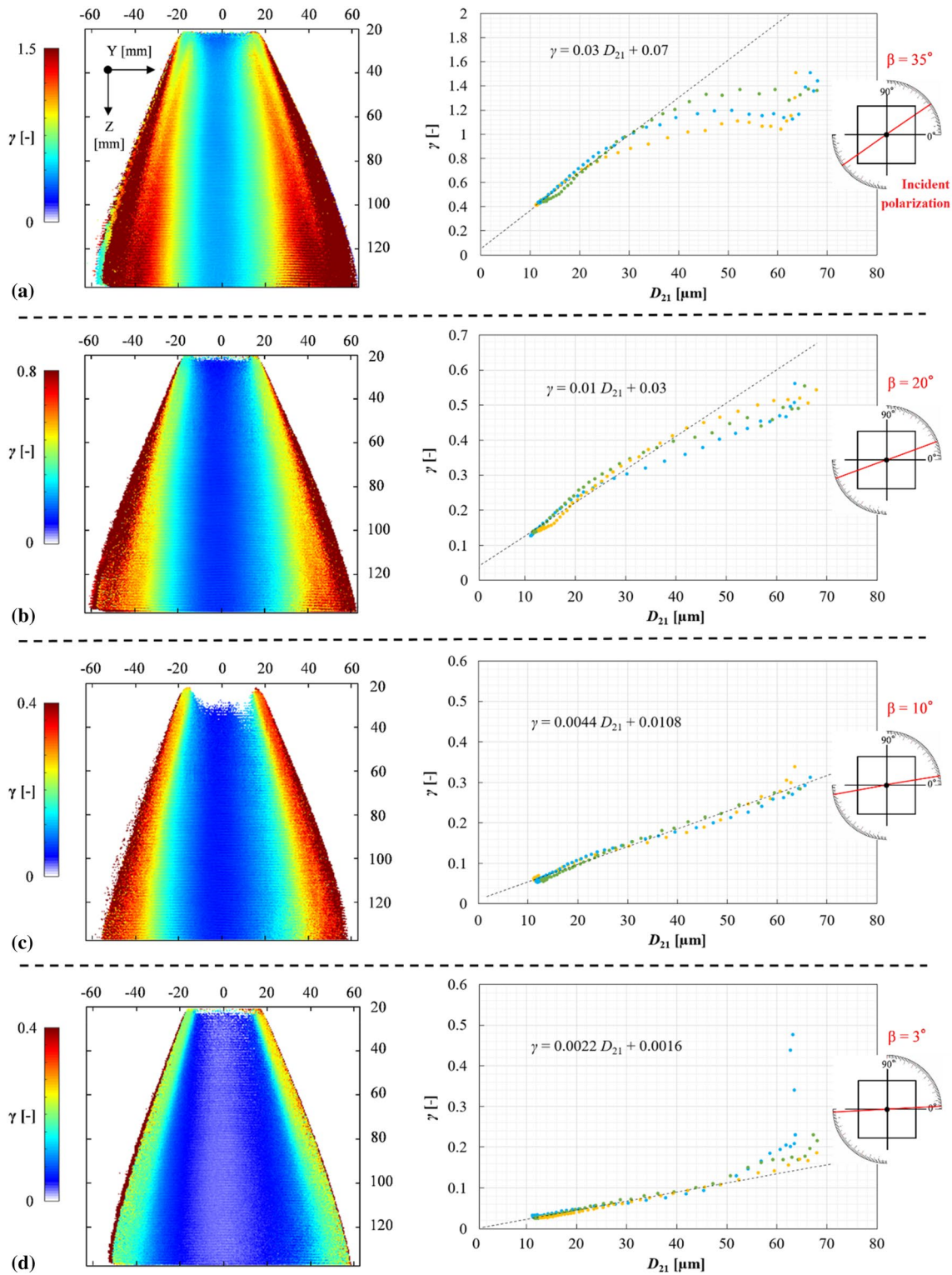


**Fig. 6** Influence of different incident light polarization ( $\beta$ =**a**  $35^\circ$ , **b**  $20^\circ$ , **c**  $10^\circ$  and **d**  $3^\circ$ ), on the polarization ratio. On the left-hand side, different average ratio maps of the water hollow-cone spray, obtained for an injection pressure of  $P_{inj}=50$  bar. The laser sheet propagates from left to right. Positions of the PDA measurement volume are dis-

played at different distances from the injector:  $Z1=50$  mm,  $Z2=70$  mm and  $Z3=90$  mm. On the right-hand side, different calibration functions correlating  $\gamma$  to the surface mean diameter  $D_{21}$  measured by PDA

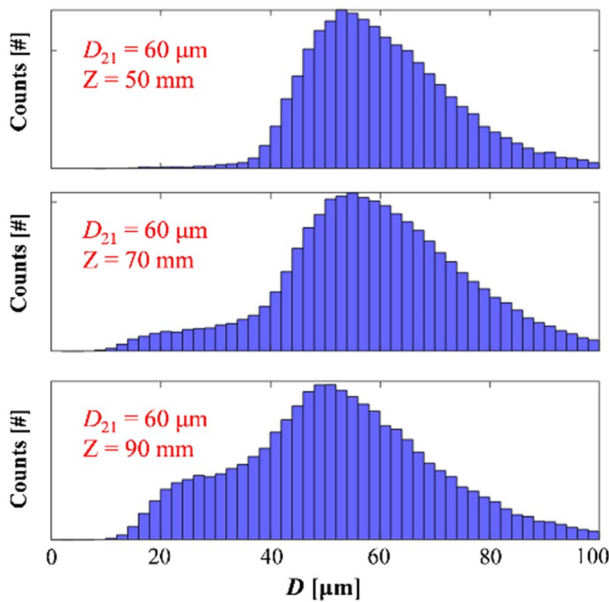


**Fig. 7** Different droplet size distributions obtained for the same  $D_{21} = 60 \mu\text{m}$  at different distances from the injector:  $Z = 50 \text{ mm}$ ,  $70 \text{ mm}$  and  $90 \text{ mm}$

$$RE = \frac{|\overline{M}_{th} - \overline{M}_{exp}|}{\overline{M}_{th}} \tag{7}$$

with  $\overline{M}_{th}$  representing the mean value of the ratio obtained from the calibration function and  $\overline{M}_{exp}$  representing the mean value of the ratio obtained from the experimental measurement.

The results are summarized in Fig. 8 for each diameter bin and each incident light polarization value. For  $\beta = 45^\circ$ , a small relative error is observed within the diameter range of  $[10\text{--}30 \mu\text{m}]$ , but the value increases significantly above  $30 \mu\text{m}$ . For  $\beta = 35^\circ$ , the maximum relative error gives less than 6.8% between 10 and  $40 \mu\text{m}$ , but beyond that, the data no longer follow the linear trend. For  $\beta = 20^\circ$  and  $10^\circ$  (Fig. 6b, c), the results show an improvement in linear trends and less discrepancy in measurements for a given diameter. However, there is still a decrease of the ratio, which varies from 0.05 to 0.35 for a diameter range from 10 to  $70 \mu\text{m}$  (Fig. 6c). The variation in  $\beta$  from  $35^\circ$  to  $10^\circ$  reduces the measurement relative error for each diameter bin, and the best result is obtained for  $\beta = 10^\circ$ : a maximum relative error of 5.6% is observed in the range  $10\text{--}70 \mu\text{m}$ . Unlike with the previous incident light polarization, here the experimental data exhibit a linear evolution across the entire data range  $[10\text{--}70 \mu\text{m}]$ . For this incident light polarization, the particle size distribution had no impact on the value of the ratio. Additionally, the dynamic ratio is sufficient for accurate measurements: the value of the ratio is multiplied by a

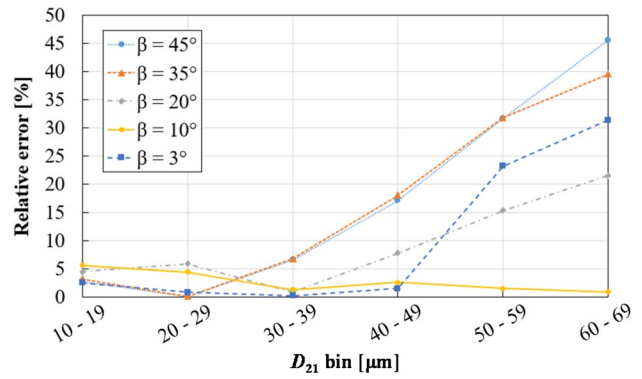


**Fig. 8** Variation in the relative error of the results observed per  $D_{21}$  range, for each incident light polarization tested

factor 3 in the range of interest. For  $\beta < 10^\circ$  (Fig. 6d), the diameter range where the relationship is linear decreases to  $[10\text{--}40 \mu\text{m}]$  and the relationship becomes nonlinear above that limit. Finally, the best result is obtained for  $\beta$  fixed at  $10^\circ$ , allowing a low relative error together with a good sensitivity of the polarization ratio measurement. The calibration function can be fitted and written:  $\gamma = 0.0044 D + 0.0108$ .

These experimental results confirm the modeling data given in (Stiti et al. 2023) which demonstrates that when the  $s$ -pol signal prevails, the fluctuation of the polarization ratio around the simulated  $D_{21}$  values is very strong. Conversely, when the  $p$ -pol signal dominates, the fluctuation is significantly attenuated. In the experiments conducted here, the ratio decreases when the  $p$ -pol signal prevails, yet the loss of linearity in the calibration function remains unexplained.

## 5 Experimental analysis of various refractive indices from the injected liquid

When considering a sphere whose diameter is much larger than the wavelength, Van de Hulst stated that most of the scattering angular pattern could be interpreted in terms of diffraction, refraction and reflection (Van de Hulst 1981). It is therefore implicit that any change in the properties of the liquid will modify electromagnetic properties such as permeability and permittivity, which affects the reflection, refraction and diffraction behavior of light in droplets. For this reason, it is important to study the influence of refractive index on the polarization ratio technique.

### 5.1 Real part of the refractive index ( $n_r$ )

With a single water droplet ( $n = 1.33 + 0i$ ), the polarization ratio technique can be used for a scattering angle in the  $75\text{--}115^\circ$  range, but beyond this limit, the ratio becomes uniform and no longer varies as a function of droplet size

(Massoli et al. 1989). Extensive work was performed by Hofeldt, in which polarization ratios were calculated for different refractive indices at a scattering angle  $\theta = 90^\circ$  (Hofeldt 1993a; b). The results show that under these scattering conditions, the technique is applicable up to a real refractive index of  $n_r = 1.40$ , but above this value, the polarization ratio varies very little with droplet size.

Experimental investigation of the dependence of the polarization ratio on the real part ( $n$ ) of the refractive index is carried out by gradually adding glycerol (Sigma Aldrich G9012) to water. For example, 20% of glycerol in water corresponds to a refractive index of  $n_r = 1.36$  and 40% of glycerol yields a refractive index of  $n_r = 1.38$ . As the viscosity of glycerol is much higher than that of water ( $\mu_{\text{glycerol}} = 1.49$  Pa.s, whereas  $\mu_{\text{water}} = 1\text{E-}3$  Pa.s), the proportion of glycerol in water is limited to a maximum of 60%, which corresponds to a real refractive index  $n_r = 1.41$ . This ensures that the water/glycerol mixture still atomizes properly. The real refractive index is then measured for each solution with an Abbe refractometer (ATAGO, DR-M2 & DR-M4). According to (Ren et al. 2012), at a wavelength of 532 nm, the imaginary part of the refractive index of the Glycerol can be considered as zero. Figure 9 presents the experimental polarization ratio obtained for different real parts of the refractive index:  $n_r =$  (a) 1.36, (b) 1.38 and (c) 1.41.

A drawback of this process is that adding glycerol to water leads to increased values of viscosity and surface tension. As a result, the particle size increases with glycerol concentration for a fixed injection pressure. In order to take account of these variations, PDA measurements are conducted for each refractive index and recorded at a distance  $Z = 70$  mm from the injector. Results are shown in Fig. 10 (cf. experimental calibration curve) and a linear calibration

function is fitted for each refractive index. The experimental results confirm the simulation performed by (Hofeldt 1993a), which showed that for a  $90^\circ$  observation angle of a polydisperse spray, the sensitivity of the ratio decreases with increasing refractive index. For a refractive index of 1.33, the ratio dynamics varies by a factor of 5 over a diameter range extending from 10 to 70  $\mu\text{m}$ , whereas a factor of 7 is observed experimentally (Hofeldt 1993a). In contrast, for a refractive index of 1.41, Hofeldt reported a factor of 2 for the same diameter range (10–70  $\mu\text{m}$ ), which is similar to our experimental results. For a refractive index of  $n = 1.33 + 0i$ , the technique is therefore more sensitive and the sensitivity of the technique decreases with increasing index. It has been numerically demonstrated that for a refractive index of 1.45, the slope becomes zero above a droplet diameter of 40  $\mu\text{m}$ , making particle size measurement impossible using the polarization ratio technique. For the experimental results obtained in this paper, the value of the slope changes from 0.0057 for a refractive index of 1.33 to a value of 0.0022 for a refractive index of 1.41. So, despite the low dynamic intensity of the ratio, the measurement is still applicable for a real refractive index value of 1.41.

To confirm the trends observed experimentally, MiePlot simulations are carried out under the same conditions and results are also displayed in Fig. 10. Six droplet size distributions were acquired with PDA. Each distribution is valid for a 10  $\mu\text{m}$  range of  $D_{21}$ : the first one for [10–20  $\mu\text{m}$ ], the second one for [20–30  $\mu\text{m}$ ], the third one for [30–40  $\mu\text{m}$ ], the fourth one for [40–50  $\mu\text{m}$ ], the fifth one for [50–60  $\mu\text{m}$ ] and the sixth one for [60–70  $\mu\text{m}$ ]. The six distributions were then used to define the mean values of  $D_{21}$  in the simulation. From these values, a numerical trend curve is reconstructed, and this process is repeated for each refractive index. The

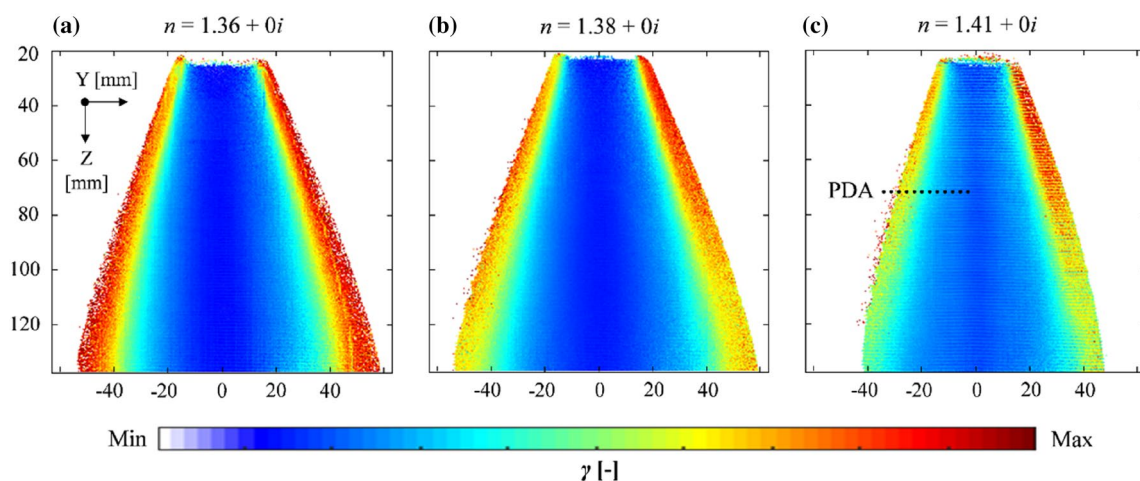


**Fig. 9** Average polarization ratio maps for different real refractive indices:  $n =$  **a** 1.33 + 0i, **b** 1.36 + 0i, **c** 1.38 + 0i and **d** 1.41 + 0i, obtained for an injection pressure of 50 bar. The laser sheet propa-

gates from left to right and the scattering angle is fixed at  $90^\circ$ . For each map, PDA measurements are realized at a distance  $Z = 70$  mm from the injector

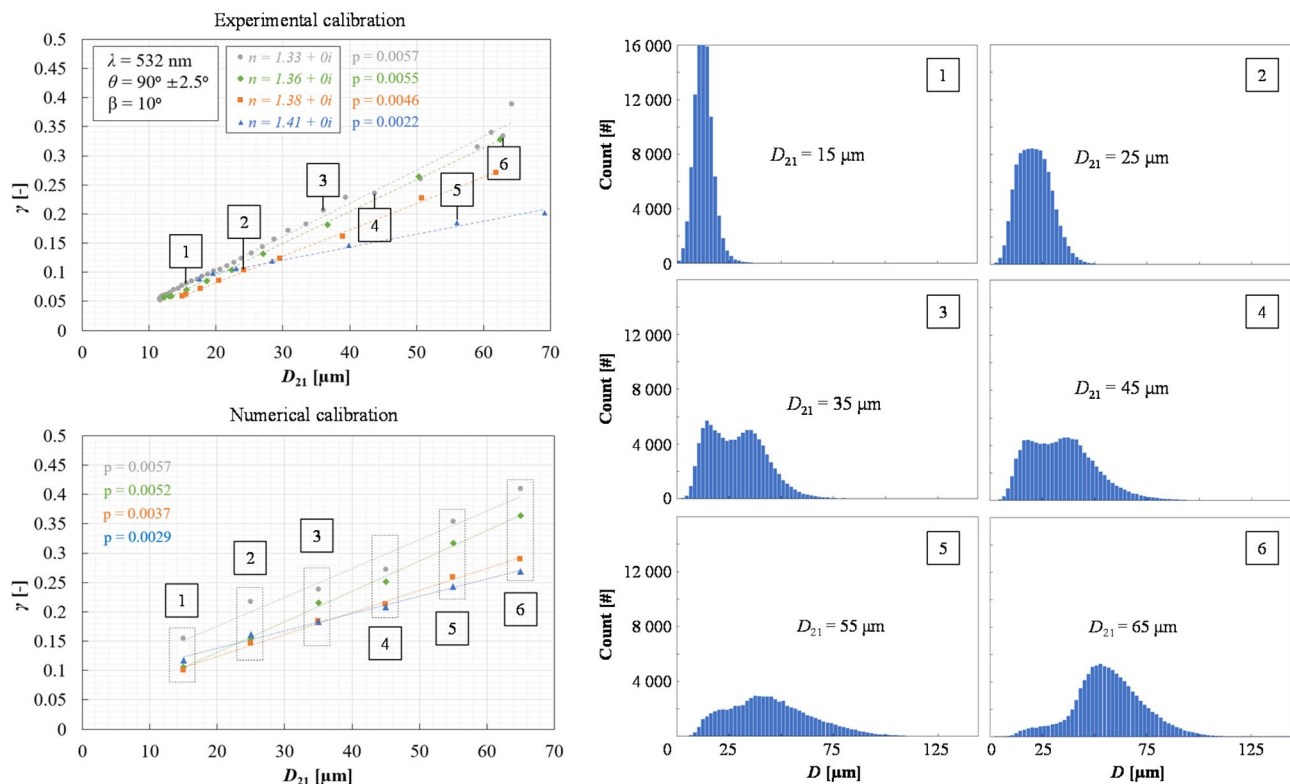


**Fig. 10** Experimental and numerical linear evolutions of the polarization ratio  $\gamma$  as a function of the surface mean diameter  $D_{21}$ , for different real refractive indices. An observation angle is set to  $90^\circ$  and the slope ( $p$ ) is defined for each refractive index. In the case of the experimental results,  $D_{21}$  has been measured by PDA at  $Z=70$  mm (refer to Fig. 9) and the incident light polarization  $\beta=10^\circ$ . Six drop-

let size distribution (PDF) obtained by PDA were used as inputs for numerical simulations, each of them attributed to a  $10 \mu\text{m}$  range of  $D_{21}$ : the first one for  $[10-20 \mu\text{m}]$ , the second one for  $[20-30 \mu\text{m}]$ , the third one for  $[30-40 \mu\text{m}]$ , the fourth one for  $[40-50 \mu\text{m}]$ , the fifth one for  $[50-60 \mu\text{m}]$  and the sixth one for  $[60-70 \mu\text{m}]$

results show a linear relationship between the ratio and the mean diameter, as well as a decrease in the value of the slope for an increase of the refractive index. Nevertheless, although the experimental and numerical slopes are quite similar for a refractive index of 1.33 and 1.36, differences can then be observed for the other refractive indices. Indeed, for a refractive index of  $n=1.38+0i$ , the experimental curve yields a slope of  $p=0.0046$  compared to a numerical slope of 0.0037. Conversely, for a refractive index of  $n=1.41+0i$ , the experimental slope ( $p=0.0022$ ) is lower than the numerical one ( $p=0.0029$ ). It has to be noted that experimental results are limited to  $n=1.41+0i$  and further investigations are required for larger refractive indices in order to verify that the slope tends toward zero.

Finally, the polarization ratio technique is applied for quantitative measurements of droplet size. The different polarization ratio mappings obtained in Fig. 9 for the three mixtures of water and glycerol are converted to  $D_{21}$  mapping. The results are presented on the left-hand side in Fig. 11. On the right-hand side, a comparison is made with PDA data, taken at the distance  $Z=70$  mm from the injector. PDA measurements are conducted along a half-spray

traverse on the incoming side of the laser sheet. Data points are collected at every two-millimeter interval, and validation is ensured with the acquisition of 100,000 droplets for each measurement point. This approach allows us to capture a maximum diameter gradient on the Y-axis, ranging from 10 to  $80 \mu\text{m}$ . As shown in Fig. 11, for the same injection pressure, the addition of glycerol in certain proportions affects the spray droplet size. Increasing the concentration of glycerol, which is more viscous than water, leads to an increase in droplet size for a fix injection pressure of 50 bar. In the case of water + 20% glycerol (Fig. 11a), the maximum  $D_{21}$  obtained is  $60 \mu\text{m}$  at the edges. In contrast, when injected with water + 60% glycerol (Fig. 11c), the  $D_{21}$  exceeds  $80 \mu\text{m}$  at the edges. This is confirmed by comparisons with PDA data, which show a measurement error of less than 4.4% for all mixtures.

## 5.2 Imaginary part of the refractive index ( $k$ )

The effects of the imaginary part of the refractive index need to be assessed in order to further investigate its influence on the polarization ratio. Some researchers have studied numerically

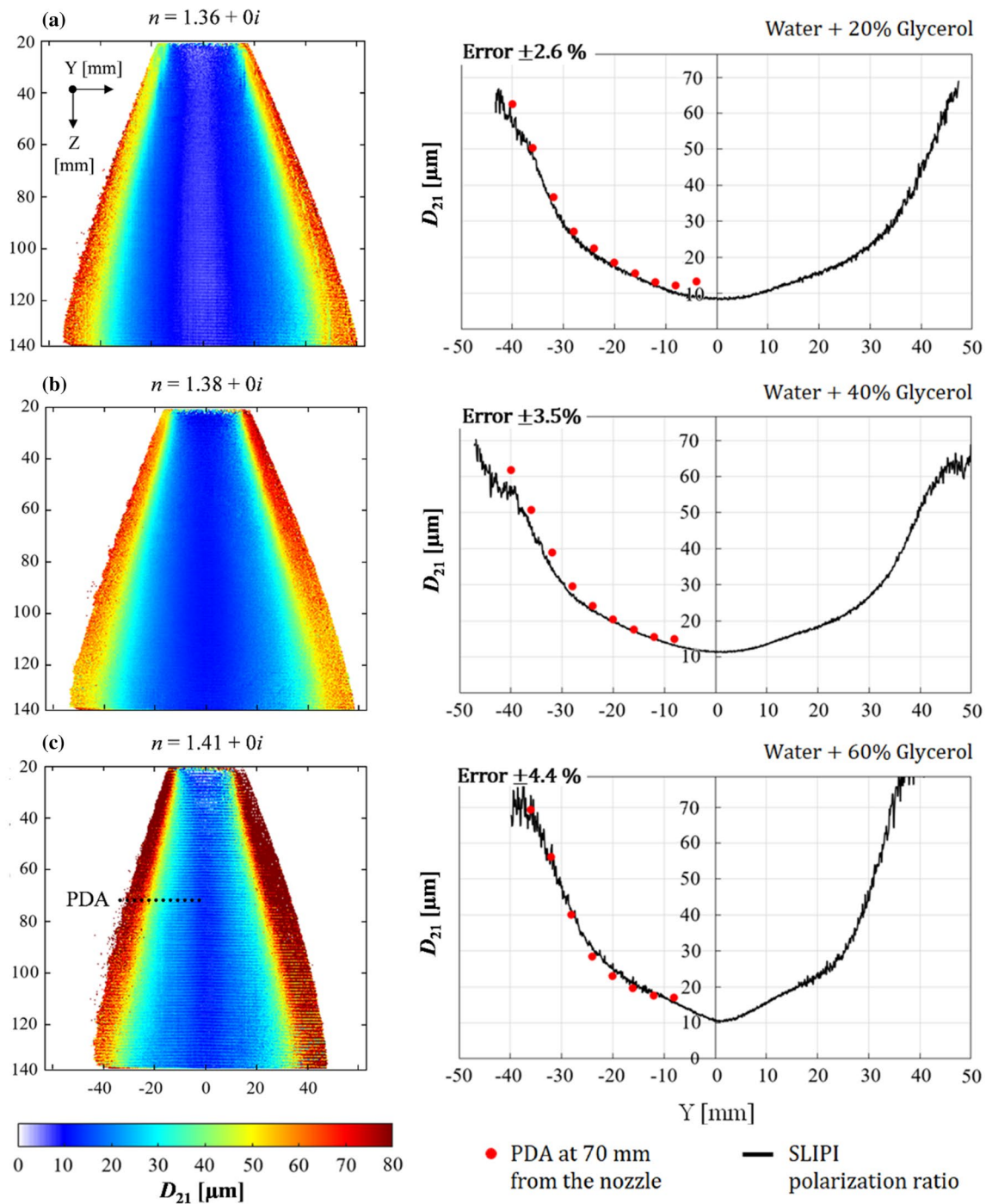


**Fig. 11** On the left-hand side, different  $D_{21}$  mappings, obtained for different refractive index: **a**  $n = 1.36 + 0i$  (water + 20% glycerol), **b**  $n = 1.38 + 0i$  (water + 40% glycerol), and **c**  $n = 1.41 + 0i$  (water + 60%

glycerol). On the right-hand side, comparison is realized between SLIPI–polarization ratio and PDA measurements of  $D_{21}$ . The average relative error is given for each case

the absorption effect on the polarization ratio technique and demonstrated that the Lorenz–Mie ripples are progressively damped as absorption increases (Beretta et al. 1985). Additional MiePlot simulations have been performed (Fig. 12), for the following experimental conditions: a scattering angle of

$90^\circ$  (with an aperture angle of  $\Delta\theta = 5^\circ$ ), a center wavelength of  $\lambda = 532$  nm, a real refractive index of  $n_r = 1.33$  and a poly-disperse droplet size distribution following a log-normal law (standard deviation of 20% and using 20 points to build the distribution), with a diameter resolution of  $\Delta D = 0.05$   $\mu\text{m}$ . As



seen in the differences between Fig. 12a, b, increasing absorption significantly reduces the Mie ripples, which confirms the results from (Beretta et al. 1985). Figure 12c presents the influence of the absorption on the polarization ratio: first, it appears that the increase of the absorption does not damp the ratio dispersion. The slope then increases with absorption, which leads to an improvement of the measurement accuracy.

Finally, the relationship between ratio and mean diameter remains linear up to an imaginary index of  $k=0.001$ , but for an index of  $k=0.002$  the relationship is no longer linear. In this case and for a range of diameters from 50 to 80  $\mu\text{m}$ , the ratio becomes almost independent of the diameter, which means that the technique is no longer suitable for droplet sizing. This shows that although it is tempting to increase absorption in order to decrease Mie ripples, the sensitivity of the polarization ratio is then reduced and limits the applicability of the technique.

## 6 Tomographic 3D reconstruction of water spray

In this last section, an average tomographic 3D map of  $D_{21}$  is obtained for a hollow-cone spray generated by the Tetra Pak injector, with an injection pressure of 50 bar. The result is obtained according to the method described in Table 1 and are presented in Fig. 13. On the top, different  $D_{21}$  half mappings used for 3D reconstruction are shown. On the middle, the 3D reconstruction method and the average 3D map of  $D_{21}$  are presented, while on the bottom, three cross-sections are derived from the 3D results, at distance  $Z_1=50$  mm,  $Z_2=80$  mm, and  $Z_3=110$  mm. All the  $D_{21}$  map used in the 3D reconstruction are obtained by applying the calibration function to convert the polarization ratio images into diameter. The results are obtained with an incident light polarization oriented at  $\beta=10^\circ$ , as recommended in the previous section (see Fig. 6c and  $\gamma=0.0044 D + 0.0108$ ). On Z-axis, the 3D map starts 50 mm downstream from the injector, where the droplets are well formed, and the Lorenz–Mie theory is applicable. At first sight, the spray appears to be symmetrical about the injector axis: larger droplets are present at the edges of the spray, whereas the smallest ones are present in the center. The hollow cone clearly appears and the  $D_{21}$  varies between a minimum value of 10  $\mu\text{m}$  in the center and more than 80  $\mu\text{m}$  at the edges. The reconstruction of a 3D map from several longitudinal 2D planes allows to obtain transverse 2D planes.

## 7 Conclusion

This paper presents an analysis of the experimental parameters influencing the application of the SLIPI–polarization ratio technique in sprays. It was first demonstrated

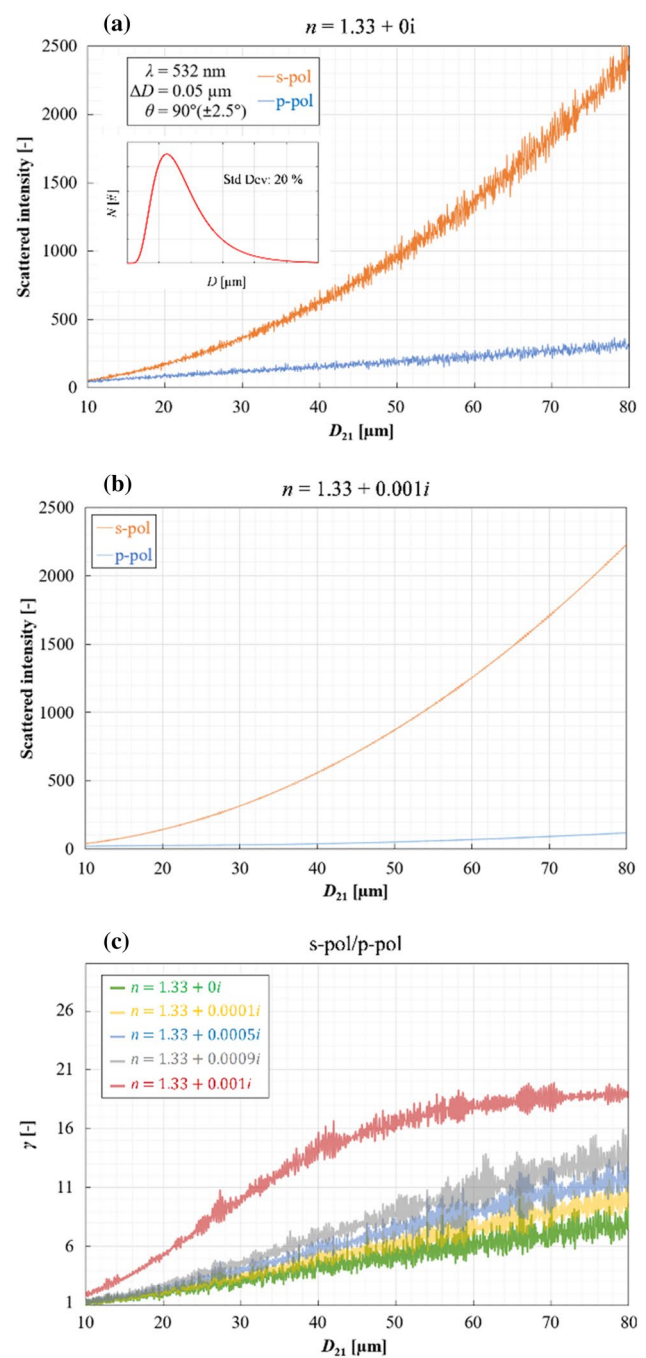


**Fig. 12** MiePlot simulation of the scattered intensity (*s-pol* and *p-pol*) function of the surface mean diameter, for two imaginary refractive indices where  $k=0$  in (a) and  $k=0.001$  in (b). The simulated conditions are similar to the experimental ones: a polydisperse spray, a scattering angle  $\theta=90^\circ$  with an opening angle  $\Delta\theta=5^\circ$ . Finally, the ratios are obtained numerically and displayed on (c)

numerically that the Lorenz–Mie ripples could be attenuated by the polydispersity of the spray, making the technique suitable for the particle sizing of an entire spray. Second, the analysis of experimental parameters has been investigated. The main results of this study can be summarized as follows:

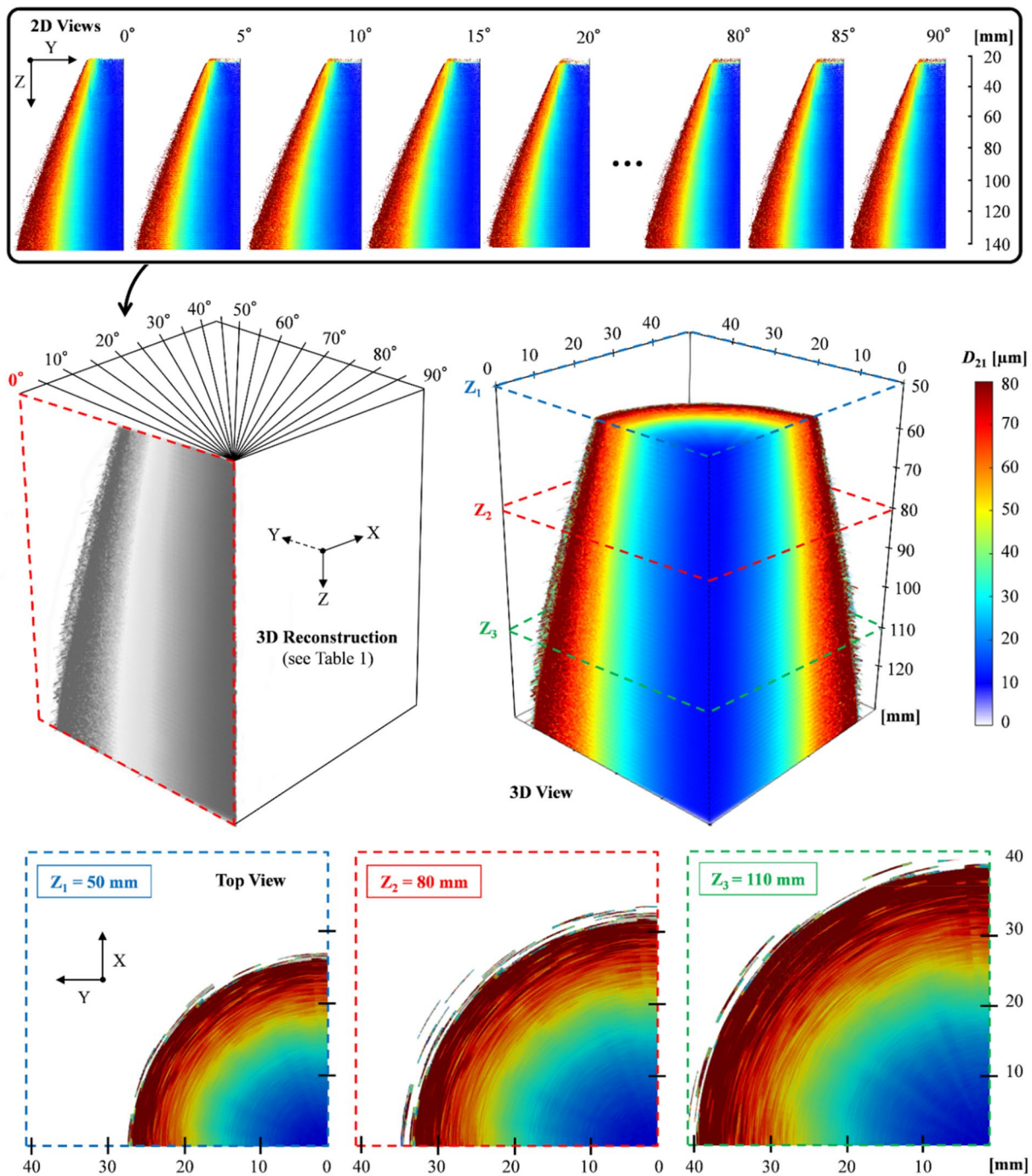


**Fig. 13** On the top side, different  $D_{21}$  half mappings are realized at different angle of the spray. These mappings are then used for the 3D reconstruction as described in in Table 1. On the middle of the figure, an average three-dimensional map of surface mean diameter  $D_{21}$

reconstructed using 2D maps is presented. The results are obtained for an injection pressure of  $P_{inj}=50$  bar. On the bottom side, three cross-sections are extracted on the studied spray, from the 3D reconstruction at distance  $Z_1=50$  mm,  $Z_2=80$  mm and  $Z_3=110$  mm

- It was found that the PDA calibration of the SLIPI-polarization ratio technique becomes fully linear for droplets between 10 and 70  $\mu\text{m}$ , when the illumination has an incident linear polarization set to 10° and 20°.
- The influence of the complex refractive index was then studied experimentally and numerically. On the one hand, the experimental results showed that for an observation angle of 90°, the technique loses its meas-

urement sensitivity when the real refractive index increases from 1.33 to 1.41. Above 1.41, it is believed that the technique may become hardly applicable for this 90° scattering angle detection. On the other hand, simulation results showed that for refractive indices above 1.41, the technique is still applicable but with a different scattering angle detection (i.e., for  $n_r = 1.41$  the most appropriate scattering angle would be 110°).

- A second numerical study was carried out to investigate the influence of the imaginary part of the refractive index (related to absorption) on the polarization ratio technique. The results showed that as the absorption effects increase, the Lorenz–Mie ripples tend to disappear. However, the relationship between  $D_{21}$  and the ratio becomes nonlinear.
- After converting the polarization ratio into  $D_{21}$  via calibration, further characterizations were carried out on sprays of water mixed with a certain proportion of glycerol (20%, 40% and 60%). These results demonstrated the reliability of the technique, giving an average relative error of less than 4.5% compared with PDA measurements.
- Finally, a 3D reconstruction of the spray diameter  $D_{21}$  was performed via tomography, enabling the overall symmetrical characterization of a hollow-cone atomizing spray that is typically used in the industry.

To conclude, SLIPI–polarization ratio provides accurate droplet sizing in 2D, in optically dense sprays. In addition, the applicability of the technique is very promising in warm and highly evaporating sprays, due to the fact that no additive dyes are needed for such measurements.

**Acknowledgements** The research leading to these results has received funding from Laserlab Europe (Grant Agreement No. 871124, European Union’s Horizon 2020 research and innovation programme). The authors gratefully acknowledge ONERA and “Région Occitanie” for PhD funding support and Tetra Pak for providing some financial support related to a spray drying project. The authors would like to also thank LaVision GmbH for providing some interest and assistance.

**Author contributions** S. Garcia wrote the manuscript text and generated the figures. M. Stiti, S. Garcia, P. Doublet and E. Berrocal contributed to the measurement system development and acquisition. C. Lempereur and M. Orain oversaw the study. All authors contributed to the field experiments and reviewed the manuscript.

**Funding** Open access funding provided by Lund University. The Swedish Research Council (Vetenskapsrådet 2021–04542) and the Lund Laser Center (grant agreement no. 871124, European Union’s Horizon 2020) are acknowledged for their financial support.

**Data availability** The data that support the findings of this study are available from the corresponding author, S. Garcia, upon reasonable request.

## Declarations

**Conflict of interest** The authors declare no conflicts of interest.

**Ethical approval** Not applicable.

**Open Access** This article is licensed under a Creative Commons Attribution 4.0 International License, which permits use, sharing, adaptation, distribution and reproduction in any medium or format, as long as you give appropriate credit to the original author(s) and the source, provide a link to the Creative Commons licence, and indicate if changes were made. The images or other third party material in this article are included in the article’s Creative Commons licence, unless indicated otherwise in a credit line to the material. If material is not included in the article’s Creative Commons licence and your intended use is not permitted by statutory regulation or exceeds the permitted use, you will need to obtain permission directly from the copyright holder. To view a copy of this licence, visit <http://creativecommons.org/licenses/by/4.0/>.

## References

- Ashgriz N (2011) Handbook of atomization and sprays: theory and applications. Springer, Boston
- Bachalo W-D (1980) Method for measuring the size and velocity of spheres by dual-beam light-scatter interferometry. *Appl Opt* 19(3):363–370
- Bachalo W, Houser L (1987) Spray drop size and velocity measurements using the phase/doppler particle analyser. *Int J Turbo Jet Engines* 4:207–215
- Bakic S et al (2008) Time integrated detection of femtosecond laser pulses scattered by small droplets. *Appl Opt*. <https://doi.org/10.1364/AO.47.000523>
- Bareiss S et al (2013) Application of femtosecond lasers to the polarization ratio technique for droplet sizing. *Meas Sci Technol* 24(2):025203
- Beretta F, Cavaliere A, D’Alessio A (1983) Experimental and theoretical analysis of the angular pattern distribution and polarization state of the light scattered by isothermal sprays and oil flames. *Combust Flame* 49(1–3):183–195
- Beretta F, Cavaliere A, D’Alessio A (1985) Ensemble laser light scattering diagnostics for the study of fuel sprays in isothermal and burning conditions. *Symp (int) Combust* 20(1):1249–1258
- Beretta F et al (1981) Laser light scattering, emission/extinction spectroscopy and thermogravimetric analysis in the study of soot behaviour in oil spray flames. *Symp (int) Combust* 18(1):1091–1096
- Berrocal E et al (2005a) Crossed source–detector geometry for a novel spray diagnostic: Monte Carlo simulation and analytical results. *Appl Optics* 44(13):2519–2529
- Berrocal E, Meglinski I, Jermy M (2005b) New model for light propagation in highly inhomogeneous polydisperse turbid media with applications in spray diagnostics. *Opt Express* 13(23):9181–9195
- Berrocal E et al (2008) Application of structured illumination for multiple scattering suppression in planar laser imaging of dense sprays. *Opt Express* 16:17870–17881
- Berrocal E et al (2012) Quantitative imaging of a non-combusting diesel spray using structured laser illumination planar imaging. *Appl Phys B* 109:683–694
- Berrocal E et al (2023) Optical spray imaging diagnostics, progress in astronautics and aeronautics. AIAA: American Institute of Aeronautics and Astronautics, Reston
- Bohren C, Huffman D (1983) Absorption and scattering of light by small particles. Wiley-VCH ed. s.l.:s.n

- Charalampous G, Hardalupas Y (2011a) Method to reduce errors of droplet sizing based on the ratio of fluorescent and scattered light intensities. *Appl Opt* 50(20):3622–3637
- Charalampous G, Hardalupas Y (2011b) Numerical evaluation of droplet sizing based on the ratio of fluorescent and scattered light intensities (LIF/Mie technique). *Appl Opt* 50:1197–1209
- Domann R, Hardalupas Y (2003) Quantitative measurement of planar droplet sauter mean diameter in sprays using planar droplet sizing. *Part Part Syst Charact* 20:209–218
- Durst F, Zaré M (1975) Laser doppler measurements in two-phase flows. *Acc Flow Meas Laser Doppler Methods*: 403429
- Frackowiak B, Tropea C (2010) Numerical analysis of diameter influence on droplet fluorescence. *Appl Opt* 49:2363–2370
- Garcia S et al (2023) Optimization of planar LIF/Mie imaging for droplet sizing characterization of dilute sprays. *Exp Fluids*. <https://doi.org/10.1007/s00348-023-03706-8>
- Hage M, Brübach J, Dreizler A (2010) Velocity and droplet diameter distributions of reacting n-heptane sprays at varied boundary conditions in a generic gas turbine combustor. *ASME Turbo Expo*, Glasgow, UK, pp 10491058
- Hofeldt D (1993a) Full-field measurements of particle size distribution: I theoretical limitations of the polarization ratio method. *Appl Opt* 32(36):7551–7558
- Hofeldt D (1993b) Full-field measurements of particle size distributions II: experimental comparison of the polarization ratio and scattered intensity methods. *Appl Opt* 32(36):7559–7567
- Hofeldt D, Hanson R (1991) Instantaneous imaging of particle size and spatial distribution in two-phase flows. *Appl Opt* 30(33):4936–4948
- Koegl M et al (2018a) Analysis of LIF and Mie signals from single micrometric droplets for instantaneous droplet sizing in sprays. *Opt Express* 26(24):31750–31766
- Koegl M et al. (2018b) D LIF/Mie planar droplet sizing in IC engine sprays using single-droplet calibration data Chicago, IL, USA, 14th ICLASS
- Koegl M et al (2019) Analysis of ethanol and butanol direct-injection spark-ignition sprays using two-phase structured laser illumination planar imaging droplet sizing. *Int J Spray Combust Dyn*. <https://doi.org/10.1177/1756827718772496>
- Koegl M et al (2022) Polarization-dependent LIF/Mie ratio for sizing of micrometric ethanol droplets doped with Nile red. *Appl Opt* 61(14):4204–4214
- Kristensson E et al (2008) High-speed structured planar laser illumination for contrast improvement of two-phase flow images. *Opt Lett* 33(23):2752–2754
- Kristensson E, Berrocal E, Richter M, Aldén M (2010) Nanosecond structured laser illumination planar imaging for single-shot imaging of dense sprays. *Atom Sprays* 20:337–343
- Lacoste J et al (2003) PDA characterisation of dense diesel sprays using a common-rail injection system. *SAE Int J Fuel Lubr* 112:2074–2085
- Laven P (2008) Simulation of rainbows, coronas, and glories by use of mie theory. *Appl Opt* 42(3):436–444
- Le Gal P, Farrugia N, Greenhalgh DA (1999) Laser sheet droplet sizing of dense sprays. *Opt Laser Technol* 31(1):75–83
- Lefebvre AH, McDonnell VG (2017) *Atomization and sprays*. CRC Press Taylor & Francis Group, Boca Raton, Florida, Etats-Unis
- Lehnert B, Weiss L, Berrocal E, Wensing M (2023) Quantifying extinction imaging of fuel sprays considering scattering errors. *Int J Eng Res* 24(10):4413–4420
- Malarski A et al (2009) The latter motivates the search for planar drop sizing (PDS) techniques as an alternative, allowing a high spatial resolution in significantly shorter measurement times. *Appl Opt* 48(10):1853–1860
- Massoli P, Beretta F, D'Alessio A (1989) Single droplet size, velocity, and optical characteristics by the polarization properties of scattered light. *Appl Opt* 28(6):1200–1205
- Mishra YN et al (2019) 3D mapping of droplet Sauter mean diameter in sprays. *Appl Opt* 58(14):3775–3783
- Mugele R, Evans HD (1951) Droplet size distribution in sprays. *Ind Eng Chem* 43:1317–1324
- Qiu S et al (2023) Droplet characteristics of multi-plume flash boiling spray evaluation using SLIPI-LIEF/Mie planar imaging technique. *Energy* 282:128876
- Rayleigh L (1878) On the instability of jets. *Proc Lond Math* 10:4–13
- Ren H, Xu S, Liu Y, Wu S-T (2012) Liquid-based infrared optical switch. *Appl Phys Lett* 101:041104
- Sankar SV, Mahleret KE, Robart DM (1999) Rapid characterization of fuel atomizers using an optical patternator. *J Eng Gas Turbines Power* 121:409–414
- Stiti M et al (2021) Characterization of supercooled droplets in an icing wind tunnel using laser-induced fluorescence. *Exp Fluids* 62:1–18
- Stiti M et al (2023) Droplet sizing in atomizing sprays using polarization ratio with structured laser illumination planar imaging. *Opt Lett* 48(15):4065–4068
- Van de Hulst H (1981) *Light scattering by small particles*. Courier Corporation
- Wellander R et al (2011) Three-dimensional measurement of the local extinction coefficient in a dense spray. *Meas Sci Technol* 22:125303
- Yeh C, Kosaka H, Kamimoto T (1993) A fluorescence/scattering imaging technique for instantaneous 2D measurement of particle size distribution in a transient spray. *Opt Part Sizing* 93:4008–4013
- Zeng W, Xu M, Zhang Y, Zhenkan W (2012) Laser sheet droplet sizing of evaporating sprays using simultaneous LIEF/Mie techniques. *Proc Combust Inst* 34:1677–1685